

ESP-MedSAM: Efficient Self-Prompting SAM for Universal Domain-Generalized Medical Image Segmentation

Qing Xu, Jiaxuan Li, Xiangjian He, *Senior Member, IEEE*, Ziyu Liu, Zhen Chen, Wenting Duan, Chenxin Li, Maggie M. He, Fiseha B. Tesema, Wooi P. Cheah, Yi Wang, Rong Qu, *Senior Member, IEEE*, Jonathan M. Garibaldi, *Fellow, IEEE*

Abstract—The universality of deep neural networks across different modalities and their generalization capabilities to unseen domains play an essential role in medical image segmentation. The recent Segment Anything Model (SAM) has demonstrated its potential in both settings. However, the huge computational costs, demand for manual annotations as prompts and conflict-prone decoding process of SAM degrade its generalizability and applicability in clinical scenarios. To address these issues, we propose an efficient self-prompting SAM for universal domain-generalized medical image segmentation, named ESP-MedSAM. Specifically, we first devise the Multi-Modal Decoupled Knowledge Distillation (MMDKD) strategy to construct a lightweight semi-parameter sharing image encoder that produces discriminative visual features for diverse modalities. Further, we introduce the Self-Patch Prompt Generator (SPPG) to automatically generate high-quality dense prompt embeddings for guiding segmentation decoding. Finally, we design the Query-Decoupled Modality Decoder (QDMD) that leverages a one-to-one strategy to provide an independent decoding channel for every modality. Extensive experiments indicate that ESP-MedSAM outperforms state-of-the-arts in diverse medical imaging segmentation tasks, displaying superior modality universality and generalization capabilities. Especially, ESP-MedSAM uses only 4.5% parameters compared to SAM-H. The source code is available at <https://github.com/xq141839/ESP-MedSAM>.

Index Terms—Medical image segmentation, knowledge distillation, domain generalization

This work is partially supported by the Yongjiang Technology Innovation Project (2022A-097-G), and the Ningbo 2025 Key R&D Project (2023Z223). (Equal contribution: Q. Xu and J. Li, Corresponding author: Xiangjian He)

Q. Xu, J. Li, X. He, Z. Liu, F. B. Tesema, W. P. Cheah and J. M. Garibaldi are with School of Computer Science, University of Nottingham Ningbo China, Ningbo, Zhejiang, China (e-mail: sean.he@nottingham.edu.cn).

Z. Chen is with Centre for Artificial Intelligence and Robotics (CAIR), Hong Kong Institute of Science & Innovation, Chinese Academy of Sciences, Hong Kong SAR.

W. Duan is with School of Computer Science, University of Lincoln, Lincoln LN6 7TS, UK.

C. Li is with Department of Electronic Engineering, The Chinese University of Hong Kong, Hong Kong 999077, SAR, China.

M. M. He is with Department of Cardiology, Gold Coast University Hospital, QLD, Australia.

Y. Wang is with School of Software, Dalian University of Technology, Dalian 116600, China.

R. Qu is with the School of Computer Science, University of Nottingham, Nottingham NG72RD, UK.

I. INTRODUCTION

MEDICAL imaging has made great strides in the last decades, spawning a variety of modalities, such as histopathology imaging, dermoscopy imaging, X-ray imaging, fundus imaging, colonoscopy imaging and ultrasound imaging. They play an important role in determining disease types and grading [1]. Traditionally, medical images are analyzed by pathologists, which is time-consuming and occupies substantial healthcare resources. In this challenging background, computer-aided diagnosis is expected to accelerate evaluation time and improve diagnostic efficiency, where pixel-level segmentation of target regions is a key step for quantitative and qualitative assessment, presenting valuable information [2].

Convolutional Neural Network (CNN) based U-shape architectures investigate the correlation between the low-level and high-level semantic information in mask prediction [3]–[6]. Although these methods demonstrate the accurate generation of segmentation masks within known domains, they are difficult to be generalized to unseen domains. To address Domain Generalization (DG) challenges, existing studies utilize multi-task learning, data augmentation and domain synthesis to improve the diversity of model feature representations [7]–[11]. However, these task-specific models require to be retrained from scratch when facing different modalities due to their limited model capacity. This raises significant challenges in establishing a segmentation model with superior generalization and universality across various medical imaging modalities.

Vision Transformer (ViT) [12] leverages the self-attention mechanism to capture long-range dependencies and provides a larger model capacity to overcome the constraints of inductive bias under the supervision of big data. Especially, the recent appearance of Segment Anything Model (SAM) [13] has made a significant breakthrough in the field of image segmentation. The superior generalization of SAM in natural images has been sufficiently validated, demonstrating its transferability in a wide range of scenarios through interactive prompts. Due to its pre-trained large-scale image encoder, current studies [14], [15] have illustrated the potential of SAM for universal domain-generalized universal medical image segmentation. Despite these advantages, adapting SAM to clinical scenarios faces three significant obstacles. Firstly, the standard SAM

[13] contains a large number of parameters. Note that the SAM-H contains 636M parameters. The huge computational costs limit the applicability of SAM in real-world scenarios. Although existing methods based on Parameter-Efficient Fine-Tuning (PEFT) techniques [16], [17] enable the reduction of learnable parameters during the fine-tuning phase, the size of the entire model is not decreased, but even increased.

Furthermore, SAM [13] mainly depends on manual annotations (e.g., points, boxes) as prompts to guide the segmentation mask generation. Although the SAM based on the bounding box prompt mode can produce relatively precise masks, it requires users to roughly provide the location of diseases in images, which can only be completed by medical experts, defeating the purpose of healthcare AI. Particularly, for the most effortless mode (i.e., single positive point) and simple automatic prompt generation algorithm, recent studies [14], [15] have indicated that they are difficult to perform acceptable results in medical applications due to insufficient or incorrect prompt information. Moreover, the original SAM [13] leverages the (modality-agnostic mask queries to predict potential segmentation masks for all categories. However, in the field of medical imaging, every vision modality has inherent heterogeneity. This many-to-many strategy is difficult to handle the mutual knowledge interference of different modalities, resulting in the degradation of model generalization.

In this paper, we propose an efficient self-prompting SAM framework for universal domain-generalized medical image segmentation, named ESP-MedSAM. Specifically, we first introduce the Multi-Modal Decoupled Knowledge Distillation (MMDKD) method to build a lightweight semi-parameter sharing image encoder that employs the modality-specific knowledge to drive the modality aggregator producing discriminative visual features across diverse modalities. Then, we devise the Self-Patch Prompt Generator (SPPG) to automatically produce a set of high-quality patch prompts assisting the prediction of segmentation masks. Moreover, we introduce the Query-Decoupled Modality Decoder (QDMD), applying the one-to-one strategy to personalise the decoding process for each medical modality, preventing the different modalities from interfering with each other.

The contributions of this work are summarized as follows.

- We propose the MMDKD strategy to distil the modality-specific and modality-common knowledge from the foundation model to a modality controller and modality aggregator, respectively. Both constitute a lightweight semi-parameter sharing image encoder, leading to the generation of distinguished features for different medical modalities.
- We devise the SPPG to produce high-quality patch prompts automatically without the demand for manual annotations. These prompts are used to guide the prediction of segmentation masks.
- We introduce the QDMD for the segmentation decoding. It leverages the one-to-one strategy to provide a private segmentation workflow to each modality, preventing the different modalities from interfering with each other.
- We take the distilled lightweight semi-parameter sharing image encoder, SPPG and QDMD to build our

ESP-MedSAM with remarkable generalization-efficiency trade-offs. We conduct extensive experiments on diverse medical imaging modalities, proving that our ESP-MedSAM outperforms state-of-the-arts in universal domain-generalized medical image segmentation.

II. RELATED WORK

A. Generalized Medical Image Segmentation

The generalization capabilities of deep neural networks have received significant attention in medical image segmentation. The original UNet [3] reveals great single-domain adaptation but is difficult to generalize unseen domains. Previous studies [4], [7], [18] mainly adopt multi-scale feature fusion to improve the feature representation power of models. In addition, Cheng *et al.* [8] utilized causality-inspired data augmentation to extend the distribution of the single-source domain during training. Xu *et al.* [9] proposed an Adversarial Domain Synthesizer (ADS) to synthesize the new domains from the memorized source domain information. As these task-specific methods have limited model capacity, they need to be trained from scratch for each modality. The recent Segment Anything Model (SAM) [13] took advantages of its large-scale image encoder and interactive prompts to achieve outstanding zero-shot generalization in natural image segmentation. In medical image segmentation, MedSAM [15] and SAMMI [14] collected more than 1M public medical images to fully fine-tune SAM with box and point prompts for domain generalized universal medical image segmentation. However, such methods rapidly increase data and computation costs, which are expensive and impractical in clinical scenarios. To mitigate the reliance on data size and computational resources during transfer learning, parameter-efficient fine-tuning techniques have been introduced in SAM. Specifically, Adapter has been widely used to integrate into the image encoder of SAM for the refinement of feature representation in medical imaging [16], [17]. SAMed [19] concatenated Low-Rank Adaptation (LoRA) with self-attention layers of SAM to optimize the feature extraction. Zhong *et al.* [20] proposed Conv-LoRA that incorporated multiple parallel convolutional experts with LoRA to sample different feature scales. While beneficial, these architectures are still based on the huge ViT encoder, which is computationally expensive. In contrast, our approach overcomes this aforementioned challenge and illustrates superior generalization-efficiency trade-offs across a variety of medical imaging modalities.

Furthermore, SAM [13] relying on laborious manual annotations as segmentation prompts seriously reduces its applicability in clinical scenarios. Although it provides a simple sliding window algorithm to automatically generate box and centre point prompts from inputs, recent studies [14], [21] have indicated that this approach fails to perform satisfactory results in medical image segmentation tasks. To minimize the need for manual annotations, SPPNet [22] computed neighbouring points around the centroid as extra prompts for nuclei image segmentation. Moreover, many studies used traditional segmentation networks (e.g., UNet [3]) to produce low-resolution masks as prompts [23]–[25]. However, such pixel-level small

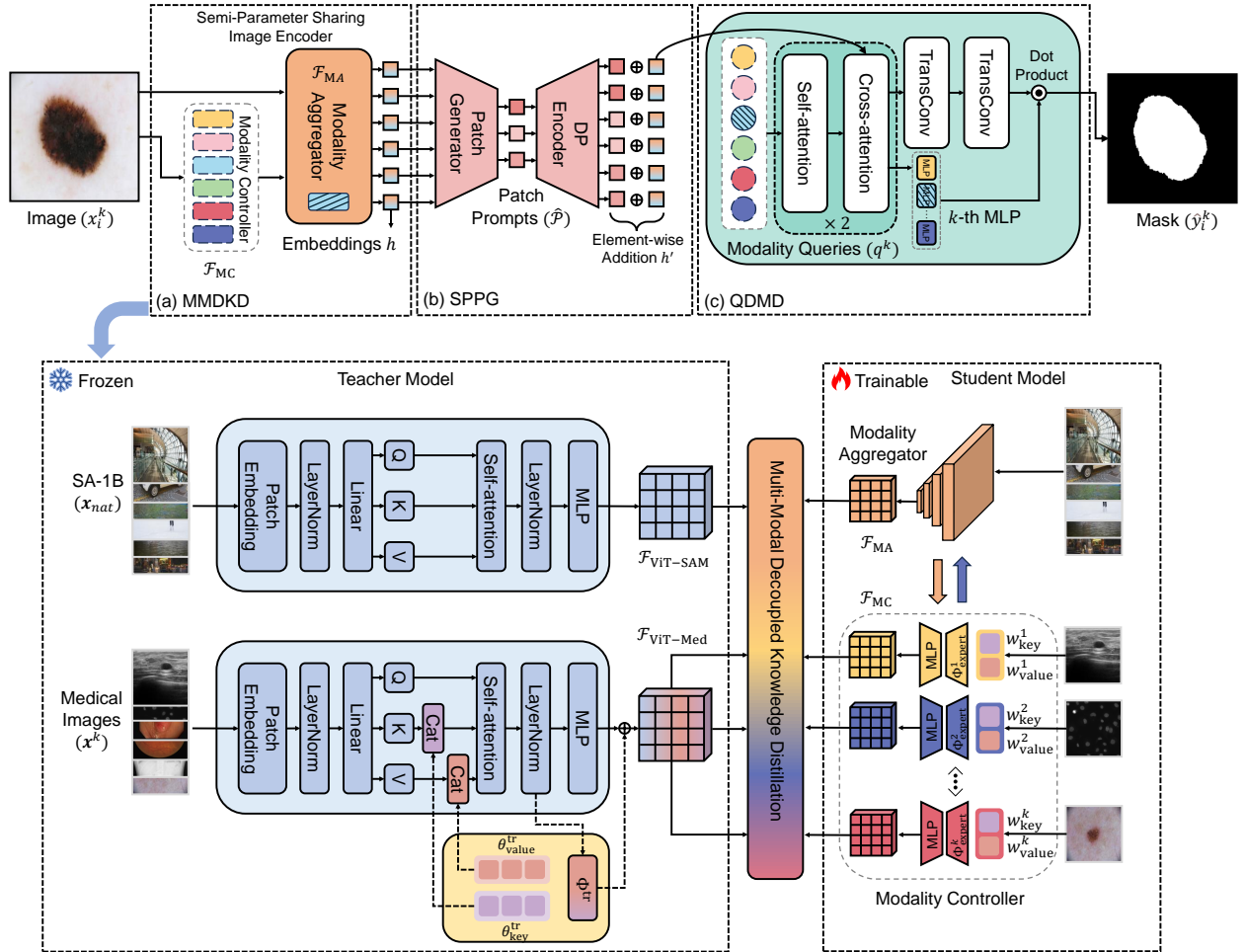


Fig. 1. The end-to-end architecture of our ESP-MedSAM for universal medical image segmentation. (a) Multi-Modal Decoupled Knowledge Distillation. (b) Self-Patch Prompt Generator. (c) Query-Decoupled Modality Decoder.

segmentors may generate more error prompts when facing heterogeneous modalities due to their limited model capacity. On the contrary, our ESP-MedSAM framework automatically generates a set of high-quality patch prompts from its own image embeddings for guiding segmentation decoding, so it eliminates the demand for labour-intensive manual annotations.

B. Knowledge Distillation

Knowledge Distillation (KD) [26] is a method of compressing the size of foundation models, transferring the knowledge from the teacher model to the student model. Generally, hard labels (e.g., category) and soft labels (e.g., probability) are used to supervise the learning of a student model from a teacher model. Yang *et al.* [27] decoupled the distillation into two stages: representation learning and classification. Subsequently, decoupled knowledge distillation [28] was introduced to divide the traditional KD loss into two parts: target class and non-target class knowledge distillation, which enhances the efficiency of knowledge transfer between the teacher and student model. In addition, it has been proven that soft labels are preferable in KD-based medical image segmentation [29]–[32]. Recently, transferring the knowledge of SAM to a

small model has become a hot research topic. MobileSAM [33] retained the prompt encoder and mask decoder of the standard SAM [13], adopting feature distillation between its image encoder and the TinyViT [34]. EdgeSAM [35] involved both the prompt encoder and mask decoder in the distillation process to capture the full knowledge embodied in SAM. EfficientSAM [36] utilised masked image pretraining method and reconstruction loss to transfer the knowledge from the image encoder of SAM to a lightweight encoder. However, these feature-coupled distillation methods are challenging to harmonise the feature representation across diverse modalities with inherent heterogeneity, resulting in the degradation of the model generalization capability. On the contrary, our method adopts a feature-level decoupled distillation strategy. The distilled image encoder enables the generation of discriminative features for different medical modalities.

III. METHODOLOGY

A. Overview of ESP-MedSAM

In this study, we denote $\mathcal{S} = \{\mathcal{S}^1, \mathcal{S}^2, \dots, \mathcal{S}^K\}$ as the set of K highly heterogeneous medical vision modalities involved in source domains. Each domain includes image and segmentation mask pairs of $\mathcal{S}^k = \{(x_i, y_i)\}_{i=1}^N$. Our goal

is to train a universal segmentation model $\mathcal{F}_\theta : x \rightarrow y$ on source domains, which not only performs well across different modalities but also can be directly generalized to an unseen target domain \mathcal{T}^k of each modality.

As presented in Fig. 1, we illustrate our ESP-MedSAM architecture for domain-generalized medical image segmentation across various modalities. Given medical images from the k -th modality, we first utilize a lightweight semi-parameter sharing image encoder to produce a set of discriminative image embeddings. This module contains two subcomponents: modality controller and modality aggregator. Both are distilled from the large ViT-based teacher model using the MMDKD strategy. Then, these embeddings are delivered to the SPPG module, which is automatically converted to a set of high-quality patch prompts to assist segmentation decoding. Finally, QDMD leverages the independent query of the corresponding modality to customize the decoding process for individual medical modalities.

B. Multi-Modal Decoupled Knowledge Distillation

SAM [13] mainly relies on a large-capacity ViT to provide generalized feature representations but is challenged by the huge computation costs, which limit its applications in real-world scenarios. Recent studies [33], [35]–[39] mainly aim to transfer the knowledge of the huge image encoder into a lightweight architecture. However, different modalities of medical imaging face inherent heterogeneity. With the reduction of model capacity, such full-parameter sharing image encoders are difficult to harmonise the feature representation of the model across diverse modalities, thereby degrading the model generalization. To address the aforementioned challenge, we propose the MMDKD to transfer the knowledge of foundation models to a lightweight semi-parameter sharing image encoder that enables generating discriminative features for different modalities, as presented in Fig. 1a.

1) *Structure of Multi-Modal Teacher Model*: To conduct the distillation process, we first construct a multi-modal teacher model that involves the natural image encoder $\mathcal{F}_{\text{ViT-SAM}}$ of SAM [13] and a medical image encoder $\mathcal{F}_{\text{ViT-Med}}$. Specifically, we freeze the weight of the image encoder in SAM and additionally create a set of learnable tokens $\{\theta_{\text{key}}^{\text{tr}}, \theta_{\text{value}}^{\text{tr}}\}$, where $\theta^{\text{tr}} \in \mathbb{R}^{t \times d}$, t and d refer to the number and dimension of tokens, respectively. They are concatenated with the *key* and *value* channels of the multi-head attention layer to learn new patterns in medical images, updating attention maps. Further, we parallelize learnable multi-layer perceptron Φ_{tr} to the Feed Forward Network (FFN) in ViT for storing diverse modality information. We take this $\mathcal{F}_{\text{ViT-Med}}$, SPPG and QDMD to implement fine-tuning on our defined medical source domains \mathcal{S} . The teacher model is supervised by a combination of focal loss and dice loss:

$$L_{\text{Mask}} = \lambda L_{\text{dice}} + (1 - \lambda) L_{\text{focal}}, \quad (1)$$

where λ represents the coefficient to adjust the weight of two loss functions. As a result, $\mathcal{F}_{\text{ViT-SAM}}$ and $\mathcal{F}_{\text{ViT-Med}}$ enable providing *modality-common knowledge* and *modality-specific knowledge*, respectively.

2) *Decoupled Knowledge Distillation*: The primary challenge in performing KD from medical foundation models to lightweight frameworks is avoiding the mutual knowledge interference of different modalities with inherent heterogeneity. Intuitively, the quality of segmentation masks depends on the feature extracted from the image encoder. Drawing inspiration from the divide-and-conquer algorithm, our proposed MMDKD method decouples the KD process into two sub-tasks: modality-common feature distillation and modality-specific feature distillation. During modality-common feature distillation, We aim to transfer the knowledge from $\mathcal{F}_{\text{ViT-SAM}}$ to a modality aggregator \mathcal{F}_{MA} . It is composed of the weights from the small ViT (e.g., TinyViT [34]). Moreover, we distil the specific knowledge of each medical modality from $\mathcal{F}_{\text{ViT-Med}}$ to the corresponding parameter bags $\{w_{\text{key}}^k, w_{\text{value}}^k, \Phi_{\text{expert}}^k\}$, where $w_{\text{key}}^k, w_{\text{value}}^k \in \mathbb{R}^{z \times d}$ are trainable tokens that respectively store the knowledge of *key* and *value* branches in $\mathcal{F}_{\text{ViT-Med}}$, and Φ_{expert}^k is MLP, with $k \in 1, 2, \dots, K$ and z being the number of tokens. All parameter bags constitute a modality controller \mathcal{F}_{MC} . The loss function of optimising these two modules is defined by:

$$L_{\text{MMDKD}} = \left\| \mathcal{F}_{\text{ViT-SAM}}(\mathbf{x}_{\text{nat}}) - \mathcal{F}_{\text{MA}}(\mathbf{x}_{\text{nat}}) \right\|_2^2 + \sum_{k=1}^K \left\| \mathcal{F}_{\text{ViT-Med}}(\mathbf{x}^k) - \mathcal{F}_{\text{MC}}(\mathbf{x}^k) \right\|_2^2, \quad (2)$$

where \mathbf{x}_{nat} stands for the 1% natural images of the SA-1B dataset [13] and \mathbf{x}^k is the medical image collected from source domains \mathcal{S}^k . The MMDKD strategy provides a private distillation channel for each medical imaging modality, preventing different modalities from interfering with each other.

3) *Lightweight Semi-Parameter Sharing Image Encoder*: To seamlessly harmonize feature representations across diverse modalities, we take the distilled modality controller and modality aggregator to build a lightweight semi-parameter sharing image encoder. Given a medical image $x_i^k \in \mathbb{R}^{H \times W \times C}$, where H , W and C are the height, width and number of channels of the image, our modality controller first send k -th parameter bag to \mathcal{F}_{MA} . Specifically, $\{w_{\text{key}}^k, w_{\text{value}}^k\}$ concatenates with \mathcal{K} and \mathcal{V} branches of the modality aggregator to adapt the attention computation \mathcal{A} of the specific modality:

$$\mathcal{A} = \text{softmax}\left(\frac{\mathcal{Q}(\mu_i^k) \cdot (\mathcal{K}(\mu_i^k) \frown w_{\text{key}}^k)^T}{\sqrt{d}}\right) \cdot (\mathcal{V}(\mu_i^k) \frown w_{\text{value}}^k), \quad (3)$$

where $\mu_i^k \in \mathbb{R}^{\frac{H \times W}{m} \times d}$ is a set of patch embeddings transformed from x_i^k with m representing the patch size, \frown is the concatenation operation, d stands for dimensions and \cdot is the matrix multiplication. Moreover, we design a residual style and combine our Φ_{expert}^k with the MLP Φ_{agg} of \mathcal{F}_{MA} to generate discriminative features for different modalities:

$$h = \mu_i^k + \mathcal{A} + \Phi_{\text{agg}}(\mathcal{F}_{\text{LN}}(\mathcal{A})) + \Phi_{\text{expert}}^k(\mathcal{F}_{\text{LN}}(\mathcal{A})), \quad (4)$$

where h is a set of image embeddings and \mathcal{F}_{LN} is LayerNorm. Overall, our proposed MMDKD method efficiently decreases the computational costs of the image encoder compared to SAM while retaining the ability to produce generalizable feature maps.

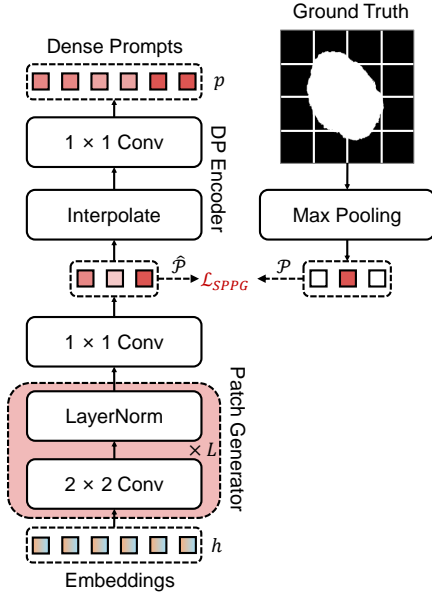


Fig. 2. The illustration of Self-Patch Prompt Generator.

C. Self-Patch Prompt Generator

Current medical SAM [14], [15], [17], [19] and lightweight SAM [33], [35]–[39] mainly leverage manual prompts (e.g., points and boxes) to guide the model providing satisfied segmentation masks. However, such methods rely on the experience of pathologists in medical scenarios, which are expensive and time-consuming. To eliminate the demand for manual annotations, we propose the SPPG that contains a patch generator and Dense Prompt (DP) encoder to automatically produce a set of high-quality patch prompts to assist segmentation decoding. As presented in Fig. 2, the patch generator δ consists of L convolutional layers for patch merging and 1×1 convolution for channel compression, where each layer includes 2×2 convolution with stride 2 followed by LayerNorm. With each additional convolutional layer, the scale of the patch is doubled. The prediction of patch prompts $\hat{\mathcal{P}}$ can be formulated as:

$$\hat{\mathcal{P}} = \frac{1}{1 + e^{(-\delta(h))}}, \quad (5)$$

where $\hat{\mathcal{P}} \in \mathbb{R}^{\frac{H \times W}{m^L}}$. As the image embedding h contains rich semantic information and the target area of many medical images is much smaller than the background, we place the patch generator on h . The patch prompt is essentially an inductive prediction, reducing the complexity of predicting the final segmentation mask by providing the summarized semantic information to the decoder. To optimize the generated patch prompts, we utilise binary cross-entropy loss to perform computation:

$$L_{\text{SPPG}} = -\frac{1}{K} \sum_{k=1}^K \mathcal{P}^k \log(\hat{\mathcal{P}}^k) + (1 - \mathcal{P}^k) \log(1 - \hat{\mathcal{P}}^k), \quad (6)$$

where \mathcal{P}^k is the target patch generated by maxpooling the ground truth of source domains \mathcal{S}^k . We then respectively use

the interpolation method for upsampling $\hat{\mathcal{P}}_k$ and 1×1 convolution to align the dimension with the image embedding h . They constitute the DP encoder. In this way, the SPPG module automatically produces a set of high-quality dense prompts p to guide the prediction of segmentation masks, improving the applicability of ESP-MedSAM in clinical scenarios.

D. Query-Decoupled Modality Decoder

The mask decoder of SAM [13] utilizes modality-agnostic query tokens to handle all segmentation tasks in natural images. However, this is not optimal for medical image segmentation. As there exists inherent heterogeneity in various medical imaging modalities, such common prediction channels suffer from decoding conflicts, degrading the generalization capabilities of the model. To address this problem, we propose the QDMD for our ESP-MedSAM framework, as provided in Fig. 1c. Concretely, we set K query tokens $\{q^k\}_{k=1}^K$, where $q^k \in \mathbb{R}^{1 \times d}$, to customize the private workflow for each Modality. We adopt a class-fixed assign algorithm where each query token corresponds to one modality category. Given the image embeddings h and prompt embeddings p , we first update the mask query: $q^k \rightarrow q_{\text{sa}}^k$ using the self-attention operation and then conduct cross-attention with the fusion of h and p : $h' \leftarrow h \oplus p$, where \oplus is an element-wise addition operation:

$$\mathcal{H} = \text{softmax}\left(\frac{(h' \oplus \Omega) \cdot (q_{\text{sa}}^k)^T}{\sqrt{d}}\right) \cdot q_{\text{sa}}^k \oplus h', \quad (7)$$

where \mathcal{H} is the decoding embedding, Ω stands for the corresponding positional encodings. Similar to SAM [13], such operations are iterated twice. To predict the segmentation mask \hat{y}_i^k , we perform:

$$\hat{y}_i^k = \sigma(\mathcal{F}_{\text{conv}}(\mathcal{H}) \cdot \Phi_{\text{dec}}^k(q_{\text{sa}}^k)), \quad (8)$$

where $\mathcal{F}_{\text{conv}}$ represents two 2×2 transpose convolutions, upsampling \mathcal{H} by $2 \times$. k -th MLP Φ_{dec}^k aligns the channel with upscaled \mathcal{H} and contains the decoding information of

TABLE I

DETAILS OF THE SOURCE DOMAINS USED IN OUR EXPERIMENTS.

No.	Dataset	Modality	Resolution	Images
\mathcal{S}^1	ISIC-2018 [40], [41]	Dermoscopy	Variable	3694
\mathcal{S}^2	PCXA [42], [43]	X-ray	Variable	704
\mathcal{S}^3	DRIVE [44]	Fundus	584×565	40
\mathcal{S}^4	CVC-ClinicDB [45]	Colonoscopy	384×288	612
\mathcal{S}^5	UDIAT [46]	Ultrasound	Variable	163
\mathcal{S}^6	DSB-2018 [47]	Microscopy	Variable	670

TABLE II

DETAILS OF THE UNSEEN DOMAINS USED IN OUR EXPERIMENTS.

No.	Dataset	Modality	Resolution	Images
\mathcal{T}^1	PH2 [48]	Dermoscopy	767×576	200
\mathcal{T}^2	NIHCXR [49]	X-ray	512×512	100
\mathcal{T}^3	STARE [50]	Fundus	700×605	20
\mathcal{T}^4	CVC-ColonDB [51]	Colonoscopy	574×500	380
\mathcal{T}^5	BUSI [52]	Ultrasound	Variable	780
\mathcal{T}^6	TNBC [53]	Microscopy	512×512	50

TABLE III
COMPARISON WITH STATE-OF-THE-ART FRAMEWORKS IN UNIVERSAL MEDICAL IMAGE SEGMENTATION (SOURCE DOMAINS).

Methods	Manual Prompt	S^1		S^2		S^3		S^4		S^5		S^6	
		Dice \uparrow	HD \downarrow	Dice \uparrow	HD \downarrow	Dice \uparrow	HD \downarrow	Dice \uparrow	HD \downarrow	Dice \uparrow	HD \downarrow	Dice \uparrow	HD \downarrow
U-Net [3]		82.87	180.90	93.85	103.51	79.13	68.22	83.91	130.96	69.24	131.62	88.16	130.28
U-Net++ [18]		82.69	175.04	95.31	75.84	80.61	65.03	85.77	152.96	72.50	137.84	90.48	112.12
Att-UNet [4]		83.97	170.78	95.80	66.16	80.72	66.48	86.90	156.72	71.02	107.70	91.12	113.64
nnUNet [5]		84.96	126.19	96.06	68.24	81.71	64.16	88.38	127.28	75.22	119.66	91.61	121.16
H2Former [6]	\times	82.12	191.39	95.54	75.44	81.46	65.09	84.66	142.08	70.30	110.98	90.17	117.69
TransUNet [54]		84.28	134.80	96.27	56.85	81.68	64.91	86.00	151.14	71.07	123.80	90.03	109.56
ADS [9]		84.14	172.84	94.89	86.68	80.48	68.49	87.70	117.74	72.55	136.08	90.32	115.24
CIAug [8]		83.91	141.07	95.82	73.18	80.45	65.72	87.69	106.68	71.78	134.84	90.58	113.72
MADGNet [7]		85.02	131.84	96.22	67.41	81.89	64.73	88.20	107.16	72.75	131.24	91.38	98.04
MobileSAM [33]		87.97	105.34	96.25	50.94	69.31	94.41	81.83	86.46	66.48	107.78	87.42	131.00
RepViT-SAM [37]		88.00	106.75	96.07	52.71	67.76	98.66	81.81	154.65	68.38	103.09	88.81	127.17
EfficientViT-SAM [38]	Point	88.49	103.61	96.43	49.07	78.16	77.16	85.16	102.72	74.71	113.18	89.37	116.42
EfficientSAM [36]		87.11	108.12	96.40	49.77	76.32	79.41	82.81	96.35	71.17	113.57	88.41	129.08
EdgeSAM [35]		88.10	100.92	96.18	51.60	68.04	92.40	81.76	105.06	67.64	105.51	87.35	113.46
SAM-Lightening [39]		88.28	101.64	96.41	50.35	74.84	87.32	83.70	97.79	73.07	129.53	89.18	111.67
MobileSAM [33]		86.19	168.48	94.75	175.50	25.56	254.24	77.29	284.32	61.51	342.22	61.49	307.44
RepViT-SAM [37]		85.73	157.66	94.27	170.27	25.10	263.76	78.75	296.36	61.62	440.75	60.54	287.63
EfficientViT-SAM [38]	\times	87.18	151.29	96.13	128.60	25.95	252.39	82.48	317.51	65.44	354.98	66.32	292.69
EfficientSAM [36]		87.02	162.45	94.89	169.20	25.84	261.51	78.54	305.36	62.05	430.18	60.56	336.55
EdgeSAM [35]		85.86	153.97	94.52	183.37	25.62	257.85	76.41	328.79	60.24	400.69	59.68	357.20
SAM-Lightening [39]		86.99	165.80	95.83	115.19	25.52	261.25	80.14	292.33	62.59	376.55	62.68	306.66
ESP-MedSAM	\times	88.52	92.42	96.83	40.68	82.42	62.64	92.93	56.32	85.28	82.32	92.24	85.93

TABLE IV
COMPARISON OF COMPUTATION COSTS WITH AUTOMATIC SEGMENTATION MODELS UNDER 1024×1024 INPUTS.

Method	Params \downarrow	FLOPs \downarrow	FPS \uparrow
U-Net [3]	13.40M	497.91G	11.07
U-Net++ [18]	9.16M	558.46G	8.57
Att-UNet [4]	8.72M	269.07G	8.45
nnUNet [5]	34.29M	554.40G	10.99
H2Former [6]	33.71M	536.96G	7.41
TransUNet [54]	109.54M	865.31G	4.73
ADS [9]	14.07M	503.59G	10.91
CIAug [8]	14.26M	500.23G	10.85
MADGNet [7]	31.40M	210.65G	8.33
MobileSAM [33]	9.79M	39.71G	1.05
RepViT-SAM [37]	9.57M	23.64G	1.12
EfficientViT-SAM [38]	34.80M	89.10G	0.91
EfficientSAM [36]	25.38M	32.51G	0.98
EdgeSAM [35]	9.60M	22.10G	1.25
SAM-Lightening [39]	19.26M	52.46G	1.02
ESP-MedSAM	28.46M	55.88G	12.87

corresponding modalities. σ stands for a sigmoid operation followed by an interpolation function that recovers the size of masks. Consequently, the proposed QDMD provides an independent decoding process for each modality, which avoids the conflicting inherent heterogeneity of different modalities, improving the generalization capabilities of our ESP-MedSAM framework.

IV. EXPERIMENTS

A. Datasets and Implementations

1) *Datasets*: To validate the effectiveness of our proposed ESP-MedSAM, we select six different medical imaging

modalities: dermoscopy, X-ray, fundus, colonoscopy, ultrasound and microscopy. Table I presents the datasets of source domains for proving the universal ability. To evaluate the domain generalizability of our framework, we further collect an external dataset for each modality, forming a set of unseen domains, as illustrated in Table II. We follow official guidelines for all datasets to create our training, validation and test sets.

2) *Implementation Details*: We perform all experiments on a single NVIDIA A6000 GPU with PyTorch. We adopt the optimizer using Adam with a learning rate of 1×10^{-4} . The batch size and epochs are set to 4 and 200, respectively. We apply the exponential decay strategy to adjust the learning rate, where the factor is set as 0.98. All images are resized to 1024×1024 during the training and test stages. We set the patch size m to be 32, $L = 1$ and utilize 1% images of the SA-1B dataset for the distillation. We use ViT-H [12] as the teacher image encoder for all SAM-based architectures. The loss coefficient λ is set to 0.7 during training. In comparing traditional automatic segmentation methods, we consider both UNet-based [3]–[6], [18], [54] and DG-based [7]–[9] fully-automated architectures as baselines. In the comparison of lightweight SAM frameworks, MobileSAM [33], RepViT-SAM [37], EfficientViT-SAM [38], EfficientSAM-Ti [36], EdgeSAM [35] and SAM-Lightening [39] are served as baselines. These architectures are trained with the point prompt mode that uses the *ConnectedComponentsWithStats* function in OpenCV to calculate the centroid of each instance as point prompts. In addition to evaluating the manual point mode, they perform the automatic mask generation mode [13].

3) *Evaluation Metrics*: To perform the comprehensive evaluation of medical image segmentation, we adopt two common metrics: Dice coefficient and Hausdorff Distance (HD). Both measure the similarity between the prediction and Ground

TABLE V

COMPARISON WITH STATE-OF-THE-ART FRAMEWORKS IN DOMAIN-GENERALIZED MEDICAL IMAGE SEGMENTATION (UNSEEN DOMAINS).

Methods	Manual Prompt	$S^1 \rightarrow T^1$		$S^2 \rightarrow T^2$		$S^3 \rightarrow T^3$		$S^4 \rightarrow T^4$		$S^5 \rightarrow T^5$		$S^6 \rightarrow T^6$	
		Dice \uparrow	HD \downarrow	Dice \uparrow	HD \downarrow	Dice \uparrow	HD \downarrow	Dice \uparrow	HD \downarrow	Dice \uparrow	HD \downarrow	Dice \uparrow	HD \downarrow
U-Net [3]		87.00	140.38	69.98	223.70	61.21	174.97	32.60	461.64	39.17	336.98	46.57	295.62
U-Net++ [18]		87.87	110.08	71.29	222.65	62.79	180.01	36.43	466.92	41.30	343.66	47.77	281.42
Att-UNet [4]		88.66	126.35	72.41	234.26	65.18	118.10	35.56	420.60	41.89	357.08	48.70	280.56
nnUNet [5]		89.56	105.53	74.48	211.68	65.00	107.82	36.00	490.92	43.87	269.04	49.19	283.67
H2Former [6]	x	87.79	146.24	73.34	219.59	65.68	115.71	34.72	480.78	42.46	275.80	53.86	294.98
TransUNet [54]		89.26	108.48	80.11	193.36	66.23	112.06	42.79	339.14	44.84	267.26	54.22	282.64
ADS [9]		87.83	129.46	76.92	180.72	62.45	172.16	37.36	454.70	43.19	276.30	51.06	281.34
CIAug [8]		88.44	127.62	68.22	257.36	65.65	120.87	39.07	387.02	41.50	267.40	53.92	286.23
MADGNet [7]		89.71	96.86	84.11	168.58	66.88	119.41	44.32	365.84	44.91	264.61	59.29	278.56
MobileSAM [33]		90.37	87.28	89.14	140.02	54.10	160.16	32.77	399.29	38.68	310.52	16.17	452.18
RepViT-SAM [37]		90.63	84.74	88.17	148.25	55.72	133.82	27.76	381.39	33.58	301.85	15.20	438.64
EfficientViT-SAM [38]	Point	91.14	85.05	89.73	145.84	72.12	116.89	61.67	179.99	58.58	183.63	34.24	332.94
EfficientSAM [36]		90.80	89.34	89.00	150.07	69.20	98.05	56.50	218.22	52.95	233.98	25.14	358.13
EdgeSAM [35]		90.38	86.32	88.01	147.62	56.03	136.48	28.17	433.08	37.51	291.65	12.11	501.14
SAM-Lightening [39]		90.85	89.96	89.63	144.84	67.38	98.85	58.12	210.20	54.75	244.37	23.69	423.15
MobileSAM [33]		85.61	304.75	87.60	277.89	2.23	253.99	20.90	470.94	31.03	342.10	6.44	375.52
RepViT-SAM [37]		84.69	283.65	86.18	290.07	2.30	283.22	17.64	491.23	26.64	409.92	5.96	383.02
EfficientViT-SAM [38]	x	89.29	177.12	89.33	287.08	9.72	256.58	58.77	357.63	46.08	501.00	14.85	442.26
EfficientSAM [36]		88.44	281.54	88.24	281.52	6.75	298.82	46.99	474.12	39.44	468.81	12.81	419.71
EdgeSAM [35]		84.31	334.93	87.07	277.67	2.37	266.70	17.64	489.03	30.01	382.82	5.83	476.44
SAM-Lightening [39]		89.41	168.96	87.62	300.50	4.26	251.03	56.94	419.96	43.68	446.36	12.01	439.31
ESP-MedSAM	x	91.45	78.13	92.24	91.30	79.68	83.84	65.96	160.13	61.62	199.74	64.21	248.47

TABLE VI

ABLATION STUDY OF ESP-MEDSAM IN DOMAIN-GENERALIZED MEDICAL IMAGE SEGMENTATION: $S \rightarrow T$.

Row	MMDKD	SPPG	QDMD	Dice (Avg.) \uparrow	HD (Avg.) \downarrow	Params \downarrow
1				64.49	451.43	90.58M
2	✓			73.81	302.72	29.08M
3		✓		69.96	152.65	90.60M
4			✓	67.28	297.51	89.94M
5	✓	✓		74.29	142.97	29.10M
6	✓		✓	75.17	272.88	28.44M
7		✓	✓	70.83	143.26	89.96M
8	✓	✓	✓	75.86	140.60	28.46M

Truth (GT), where HD is more sensitive to the boundary than Dice. We also report model parameters, Floating Point Operations (FLOPs) and Frames Per Second (FPS) to reveal the computation costs. To match the predicted K masks with the corresponding ground truth y_i^k , we calculate the Dice score between $\{\hat{y}_i^k\}_{k=1}^K$ and y_i^k . The one with the highest Dice score in this set is chosen as the matching prediction mask for the following evaluation of segmentation [14].

B. Comparison on Universal Medical Image Segmentation

To validate the effectiveness of our lightweight ESP-MedSAM framework in universal medical instance segmentation, we compare it with SOTA fully-automated architectures: U-Net [3], U-Net++ [18], Att-UNet [4], nnUNet [5], H2Former [6], TransUNet [54], ADS [9], CIAug [8], MADGNet [7] and lightweight SAMs [33], [35]–[39] on source domains of six medical imaging modalities, as illustrated in Table III. For fair comparisons, the knowledge of lightweight SAMs is distilled from the same teacher model $\mathcal{F}_{ViT-Med}$. Firstly, it can be observed that ESP-MedSAM performs better than all task-specific models, especially achieving

a Dice of 85.28% in S^5 and being 10.06% higher than nnUNet [5]. Note that all task-specific models require to be retrained on each domain. Therefore, our ESP-MedSAM demonstrates outstanding universal capabilities. Secondly, compared to recent lightweight SAMs, the proposed ESP-MedSAM outperforms the laborious point-prompt mode. Particularly, with the automatic mask generation mode, the performance of these lightweight SAMs in retinal vessel and nuclei segmentation tasks declines rapidly. The proposed ESP-MedSAM significantly surpasses EfficientViT-SAM [38] with a 56.47% and 25.92% Dice increase, respectively. On HD metric, our framework reduces the distance by up to $5.8\times$ compared to current SOTA models, revealing more accurate boundary prediction. Furthermore, we present the computation costs of each framework in Table IV. In high-resolution medical image segmentation tasks, we observe that traditional task-specific architectures demonstrate acceptable inference speed but higher model complexity. The recent lightweight SAMs suffer from the slow inference speed in the automatic mask generation mode due to the inefficient sliding window algorithm. In contrast, our ESP-MedSAM displays remarkable complexity-speed trade-offs. These results reveal the superior universal capabilities of our ESP-MedSAM on diverse medical segmentation tasks without the demand for manual prompts.

C. Comparison on Domain-Generalized Medical Image Segmentation

Furthermore, we evaluate the generalization capabilities of our ESP-MedSAM architecture on unseen target domains, which is provided in Table V. Within task-specific architectures, the large-capacity TransUNet [54] and multi-task learning MADGNet [7] show better performance than nnUNet [5]. On the contrary, our method achieves overwhelming performance on all unseen domains with a significant rise

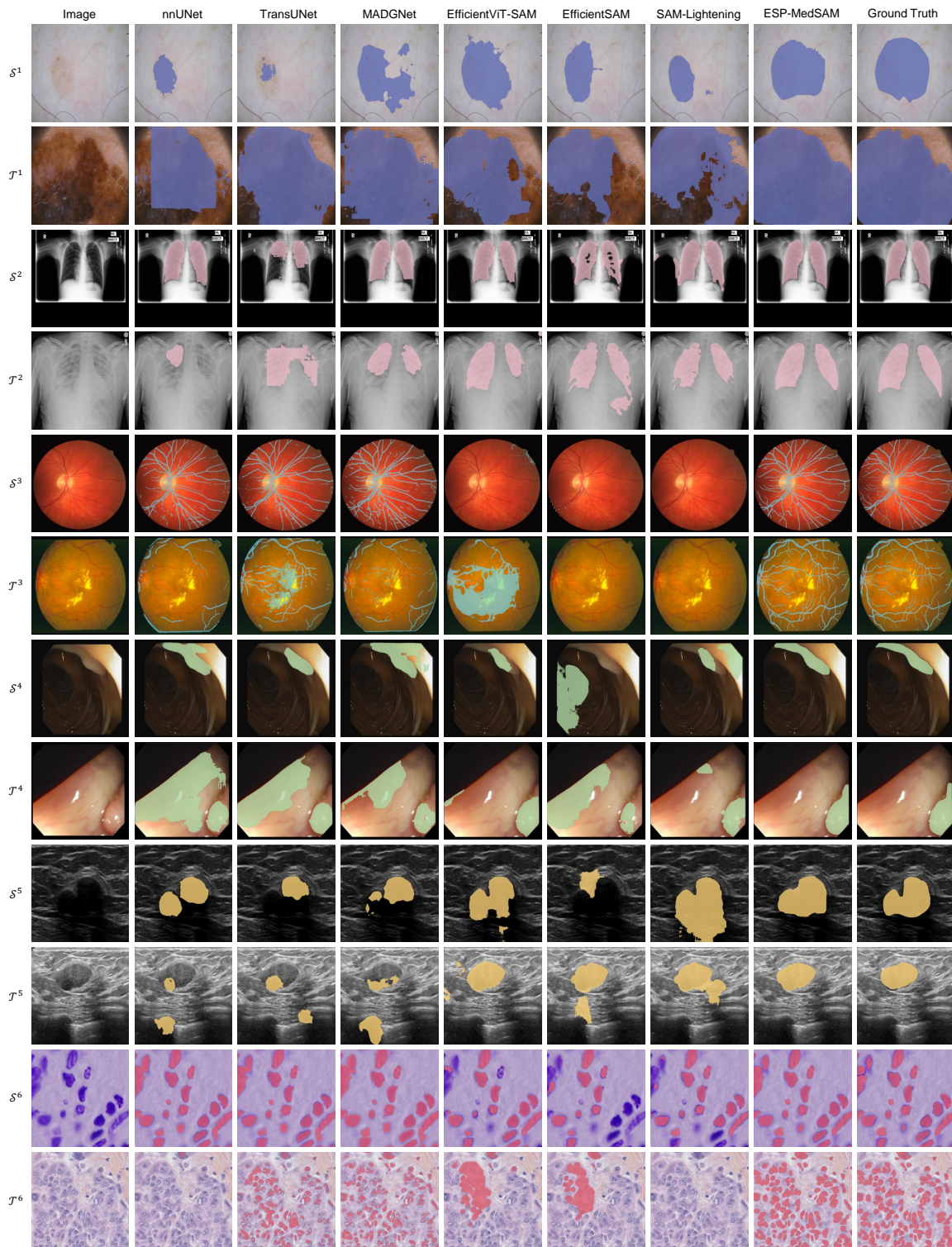


Fig. 3. Qualitative comparison with SOTA task-specific models and lightweight SAM frameworks with the automatic mask generation mode on medical image segmentation over source and unseen target domains of six modalities.

of 1.74%, 8.13%, 12.80%, 21.64%, 16.71% and 4.92% over MADGNet on the Dice metric. Compared to the lightweight SAMs, the proposed ESP-MedSAM tackle the challenge of segmentation mask generations in retinal vessels, ultrasound cancer and microscopic nuclei segmentation tasks, improving the Dice score by more than 50%. Remarkably, our ESP-

MedSAM framework illustrates a lower HD distance, which provides a more precise localization for segmentation targets. Overall, these results demonstrate the superior generalization capabilities of the proposed ESP-MedSAM on unseen domains of different medical modalities while eliminating the demand for manual prompts.

D. Ablation Study

To investigate the effectiveness of MMDKD, SPPG and QDMD modules, we further conduct a comprehensive ablation study on unseen target domains of six medical imaging modalities, displayed in Table VI. By removing the devised modules from ESP-MedSAM, in 1st row, the standard fine-tuned SAM [13] serves as the ablation baseline. By separately adding the MMDKD (2nd row), SPPG (3rd row) and QDMD (4th row), the performance is increased with the average Dice of all modalities gain of 9.32%, 5.47%, 2.79%, respectively. Particularly, the MMDKD strategy decreases 67.90% of the parameters compared to SAM. The introducing SPPG module (3rd row) significantly reduces HD by 66.19%, which is more efficient than manual point prompts. The 5th row to the 7th row indicate the compatibility between each module. Overall, these ablation experiments prove that the MMDKD strategy significantly decreases the computation costs of ESP-MedSAM. SPPG eliminates the requirement for manual annotations. QDMD further enhances the generalization capabilities of the model across diverse modalities.

E. Discussion

1) *Effectiveness of Patch Prompt Learning*: In this section, we delve into the rationale behind the adoption of the patch prompt learning strategy. Initially, we examine the efficiency of SPPG with different patch sizes on source domains. As illustrated in Fig. 4 (left), based on the average performance on six modalities, setting a relatively large patch size proves beneficial for the patch category task, albeit it provides less semantic information than mask prompts. Conversely, reducing the patch size increases the prediction complexity, consequently leading to more errors or noise. Additionally, we conduct a comparison of our devised patch prompt with point, box and Low-Resolution (LR) mask prompt modes in Fig. 4 (right). Considering that automatic prompt generation aims to learn the representation of human annotations, all prompt types utilize manual annotations (ground truth) as inputs for the experiment. Observations reveal that the manual patch prompt outperforms both the box and point prompts. Therefore, the learning patch prompt approach proves more efficient for guiding the segmentation decoding.

2) *Significance of Decoupling Strategy*: In the design of the MMDKD strategy, we adopt a decoupling strategy to provide an independent encoding workflow for each modality. To qualitatively evaluate the effectiveness of ESP-MedSAM in learning discriminative representations, we make a feature comparison via T-SNE with the baseline (using a full-parameter sharing strategy). As shown in Fig. 5, the features produced by our method exhibit significant discriminability over the six medical image modalities on unseen domains, which benefits the following decoder in terms of segmentation masks significantly, enhancing the universal and generalized capabilities of ESP-MedSAM.

V. CONCLUSION

In this paper, we have proposed the ESP-MedSAM framework for universal medical image segmentation. Specifically,

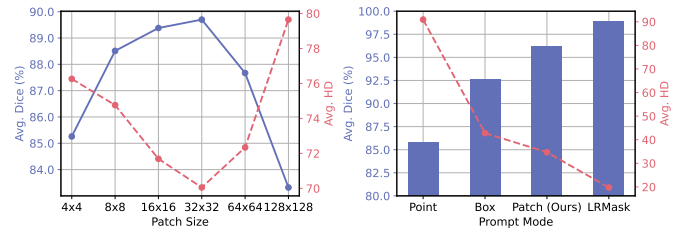


Fig. 4. Hyper-parameter analysis of patch size (left) and comparison of model performance based on different prompt types (right). Each prompt type utilizes manual annotations (ground truth) as the input.

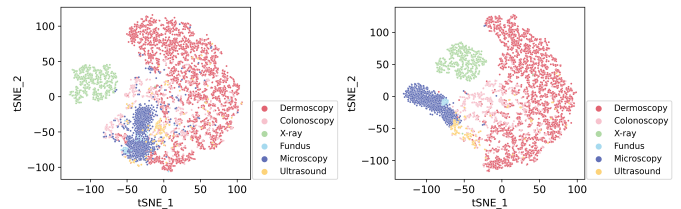


Fig. 5. Feature comparison via T-SNE between the baseline model and our ESP-MedSAM framework on unseen target domains.

The MMDKD strategy has been introduced to distill the knowledge from the foundation model to a modality controller and a modality controller to create a semi-parameter sharing image encoder for discriminative feature generation. Then, SPPG has been devised to automatically produce a set of high-quality patch prompts for assisting segmentation decoding. Finally, QDMD has customized a specific segmentation workflow for each modality. Extensive experiments have demonstrated that ESP-MedSAM has lower computational complexity than the standard SAM and outperforms SOTA task-specific architectures and lightweight SAMs in diverse medical imaging segmentation tasks, exhibiting superior zero-shot generalization and universal capabilities.

REFERENCES

- [1] I. Qureshi, J. Yan, Q. Abbas, K. Shaheed, A. B. Riaz, A. Wahid, M. W. J. Khan, and P. Szczuko, "Medical image segmentation using deep semantic-based methods: A review of techniques, applications and emerging trends," *Inf. Fusion*, vol. 90, pp. 316–352, 2023.
- [2] G. Litjens, T. Kooi, B. E. Bejnordi, A. A. A. Setio, F. Ciompi, M. Ghafoorian, J. A. Van Der Laak, B. Van Ginneken, and C. I. Sánchez, "A survey on deep learning in medical image analysis," *Med. Image Anal.*, vol. 42, pp. 60–88, 2017.
- [3] O. Ronneberger, P. Fischer, and T. Brox, "U-net: Convolutional networks for biomedical image segmentation," in *MICCAI*. Springer, 2015, pp. 234–241.
- [4] J. Schlemper, O. Oktay, M. Schaap, M. Heinrich, B. Kainz, B. Glocker, and D. Rueckert, "Attention gated networks: Learning to leverage salient regions in medical images," *Med. Image Anal.*, vol. 53, pp. 197–207, 2019.
- [5] F. Isensee, P. F. Jaeger, S. A. Kohl, J. Petersen, and K. H. Maier-Hein, "nnu-net: a self-configuring method for deep learning-based biomedical image segmentation," *Nature Methods*, vol. 18, no. 2, pp. 203–211, 2021.
- [6] A. He, K. Wang, T. Li, C. Du, S. Xia, and H. Fu, "H2former: An efficient hierarchical hybrid transformer for medical image segmentation," *IEEE Trans. Med. Imaging*, vol. 42, no. 9, pp. 2763–2775, 2023.
- [7] J.-H. Nam, N. S. Syazwany, S. J. Kim, and S.-C. Lee, "Modality-agnostic domain generalizable medical image segmentation by multi-frequency in cross-scale attention," in *CVPR*, 2024, pp. 11 480–11 491.
- [8] C. Ouyang, C. Chen, S. Li, Z. Li, C. Qin, W. Bai, and D. Rueckert, "Causality-inspired single-source domain generalization for medical image segmentation," *IEEE Trans. Med. Imaging*, vol. 42, no. 4, pp. 1095–1106, 2022.

- [9] Y. Xu, S. Xie, M. Reynolds, M. Ragoza, M. Gong, and K. Batmanghelich, "Adversarial consistency for single domain generalization in medical image segmentation," in *MICCAI*. Springer, 2022, pp. 671–681.
- [10] C. Li, W. Ma, L. Sun, X. Ding, Y. Huang, G. Wang, and Y. Yu, "Hierarchical deep network with uncertainty-aware semi-supervised learning for vessel segmentation," *Neural Comput. Appl.*, pp. 1–14.
- [11] C. Li, Y. Zhang, Z. Liang, W. Ma, Y. Huang, and X. Ding, "Consistent posterior distributions under vessel-mixing: a regularization for cross-domain retinal artery/vein classification," in *ICIP*. IEEE, 2021, pp. 61–65.
- [12] A. Dosovitskiy, L. Beyer, A. Kolesnikov, D. Weissenborn, X. Zhai, T. Unterthiner, M. Dehghani, M. Minderer, G. Heigold, S. Gelly *et al.*, "An image is worth 16x16 words: Transformers for image recognition at scale," in *ICLR*, 2020.
- [13] A. Kirillov, E. Mintun, N. Ravi, H. Mao, C. Rolland, L. Gustafson, T. Xiao, S. Whitehead, A. C. Berg, W.-Y. Lo, P. Dollar, and R. Girshick, "Segment anything," in *ICCV*, October 2023, pp. 4015–4026.
- [14] Y. Huang, X. Yang, L. Liu, H. Zhou, A. Chang, X. Zhou, R. Chen, J. Yu, J. Chen, C. Chen *et al.*, "Segment anything model for medical images?" *Med. Image Anal.*, vol. 92, p. 103061, 2024.
- [15] J. Ma, Y. He, F. Li, L. Han, C. You, and B. Wang, "Segment anything in medical images," *Nature Communications*, vol. 15, no. 1, p. 654, 2024.
- [16] X. Lin, Y. Xiang, L. Zhang, X. Yang, Z. Yan, and L. Yu, "Samus: Adapting segment anything model for clinically-friendly and generalizable ultrasound image segmentation," *arXiv preprint arXiv:2309.06824*, 2023.
- [17] J. Wu, W. Ji, Y. Liu, H. Fu, M. Xu, Y. Xu, and Y. Jin, "Medical sam adapter: Adapting segment anything model for medical image segmentation," *arXiv preprint arXiv:2304.12620*, 2023.
- [18] Z. Zhou, M. M. R. Siddiquee, N. Tajbakhsh, and J. Liang, "Unet++: Redesigning skip connections to exploit multiscale features in image segmentation," *IEEE Trans. Med. Imaging*, vol. 39, no. 6, pp. 1856–1867, 2019.
- [19] K. Zhang and D. Liu, "Customized segment anything model for medical image segmentation," *arXiv preprint arXiv:2304.13785*, 2023.
- [20] Z. Zhong, Z. Tang, T. He, H. Fang, and C. Yuan, "Convolution meets lora: Parameter efficient finetuning for segment anything model," in *ICLR*, 2024.
- [21] M. A. Mazurowski, H. Dong, H. Gu, J. Yang, N. Konz, and Y. Zhang, "Segment anything model for medical image analysis: an experimental study," *Med. Image Anal.*, vol. 89, p. 102918, 2023.
- [22] Q. Xu, W. Kuang, Z. Zhang, X. Bao, H. Chen, and W. Duan, "Sppnet: A single-point prompt network for nuclei image segmentation," in *MICCAI Workshop on MLMI*. Springer, 2023, pp. 227–236.
- [23] X. Zhang, Y. Liu, Y. Lin, Q. Liao, and Y. Li, "Uv-sam: Adapting segment anything model for urban village identification," in *AAAI*, vol. 38, no. 20, 2024, pp. 22 520–22 528.
- [24] Z. Cheng, Q. Wei, H. Zhu, Y. Wang, L. Qu, W. Shao, and Y. Zhou, "Unleashing the potential of sam for medical adaptation via hierarchical decoding," *CVPR*, 2024.
- [25] Y. Gu, Q. Wu, H. Tang, X. Mai, H. Shu, B. Li, and Y. Chen, "Lesam: Adapt segment anything model for medical lesion segmentation," *IEEE J. Biomed. Health Inform.*, 2024.
- [26] G. Hinton, O. Vinyals, and J. Dean, "Distilling the knowledge in a neural network," *arXiv preprint arXiv:1503.02531*, 2015.
- [27] J. Yang, B. Martinez, A. Bulat, and G. Tzimiropoulos, "Knowledge distillation via softmax regression representation learning," in *ICLR*, 2020.
- [28] B. Zhao, Q. Cui, R. Song, Y. Qiu, and J. Liang, "Decoupled knowledge distillation," in *CVPR*, 2022, pp. 11 953–11 962.
- [29] D. Qin, J.-J. Bu, Z. Liu, X. Shen, S. Zhou, J.-J. Gu, Z.-H. Wang, L. Wu, and H.-F. Dai, "Efficient medical image segmentation based on knowledge distillation," *IEEE Trans. Med. Imaging*, vol. 40, no. 12, pp. 3820–3831, 2021.
- [30] Q. Zhao, L. Zhong, J. Xiao, J. Zhang, Y. Chen, W. Liao, S. Zhang, and G. Wang, "Efficient multi-organ segmentation from 3d abdominal ct images with lightweight network and knowledge distillation," *IEEE Trans. Med. Imaging*, 2023.
- [31] H. Wu, Z. Wang, Z. Zhao, C. Chen, and J. Qin, "Continual nuclei segmentation via prototype-wise relation distillation and contrastive learning," *IEEE Trans. Med. Imaging*, 2023.
- [32] C. Li, M. Lin, Z. Ding, N. Lin, Y. Zhuang, Y. Huang, X. Ding, and L. Cao, "Knowledge condensation distillation," in *European Conference on Computer Vision*. Springer, 2022, pp. 19–35.
- [33] C. Zhang, D. Han, Y. Qiao, J. U. Kim, S.-H. Bae, S. Lee, and C. S. Hong, "Faster segment anything: Towards lightweight sam for mobile applications," *arXiv preprint arXiv:2306.14289*, 2023.
- [34] K. Wu, J. Zhang, H. Peng, M. Liu, B. Xiao, J. Fu, and L. Yuan, "Tinyvit: Fast pretraining distillation for small vision transformers," in *ECCV*. Springer, 2022, pp. 68–85.
- [35] C. Zhou, X. Li, C. C. Loy, and B. Dai, "Edgesam: Prompt-in-the-loop distillation for on-device deployment of sam," *arXiv preprint arXiv:2312.06660*, 2023.
- [36] Y. Xiong, B. Varadarajan, L. Wu, X. Xiang, F. Xiao, C. Zhu, X. Dai, D. Wang, F. Sun, F. Iandola *et al.*, "Efficientsam: Leveraged masked image pretraining for efficient segment anything," *CVPR*, 2024.
- [37] A. Wang, H. Chen, Z. Lin, J. Han, and G. Ding, "Repvit-sam: Towards real-time segmenting anything," *CVPR*, 2024.
- [38] Z. Zhang, H. Cai, and S. Han, "Efficientvit-sam: Accelerated segment anything model without performance loss," *arXiv preprint arXiv:2402.05008*, 2024.
- [39] Y. Song, B. Pua, P. Wanga, H. Jiang, D. Donga, and Y. Shen, "Sam-lightening: A lightweight segment anything model with dilated flash attention to achieve 30 times acceleration," *arXiv preprint arXiv:2403.09195*, 2024.
- [40] P. Tschandl, C. Rosendahl, and H. Kittler, "The ham10000 dataset, a large collection of multi-source dermatoscopic images of common pigmented skin lesions," *Sci. Data*, vol. 5, no. 1, pp. 1–9, 2018.
- [41] N. Codella, V. Rotemberg, P. Tschandl, M. E. Celebi, S. Dusza, D. Gutman, B. Helba, A. Kalloo, K. Liopyris, M. Marchetti *et al.*, "Skin lesion analysis toward melanoma detection 2018: A challenge hosted by the international skin imaging collaboration (isic)," *arXiv preprint arXiv:1902.03368*, 2019.
- [42] S. Jaeger, A. Karargyris, S. Candemir, L. Folio, J. Siegelman, F. Callaghan, Z. Xue, K. Palaniappan, R. K. Singh, S. Antani *et al.*, "Automatic tuberculosis screening using chest radiographs," *IEEE Trans. Med. Imaging*, vol. 33, no. 2, pp. 233–245, 2013.
- [43] S. Candemir, S. Jaeger, K. Palaniappan, J. P. Musco, R. K. Singh, Z. Xue, A. Karargyris, S. Antani, G. Thoma, and C. J. McDonald, "Lung segmentation in chest radiographs using anatomical atlases with nonrigid registration," *IEEE Trans. Med. Imaging*, vol. 33, no. 2, pp. 577–590, 2013.
- [44] J. Staal, M. D. Abràmoff, M. Niemeijer, M. A. Viergever, and B. Van Ginneken, "Ridge-based vessel segmentation in color images of the retina," *IEEE Trans. Med. Imaging*, vol. 23, no. 4, pp. 501–509, 2004.
- [45] J. Bernal, F. J. Sánchez, G. Fernández-Esparrach, D. Gil, C. Rodríguez, and F. Vilariño, "Wm-dova maps for accurate polyp highlighting in colonoscopy: Validation vs. saliency maps from physicians," *Comput. Med. Imaging Graph.*, vol. 43, pp. 99–111, 2015.
- [46] M. H. Yap, G. Pons, J. Marti, S. Ganau, M. Sents, R. Zwigelaar, A. K. Davison, and R. Marti, "Automated breast ultrasound lesions detection using convolutional neural networks," *IEEE J. Biomed. Health Inform.*, vol. 22, no. 4, pp. 1218–1226, 2017.
- [47] J. C. Caicedo, A. Goodman, K. W. Karhohs, B. A. Cimini, J. Ackerman, M. Haghghi, C. Heng, T. Becker, M. Doan, C. McQuin *et al.*, "Nucleus segmentation across imaging experiments: the 2018 data science bowl," *Nature Methods*, vol. 16, no. 12, pp. 1247–1253, 2019.
- [48] T. Mendonça, P. M. Ferreira, J. S. Marques, A. R. Marcal, and J. Rozeira, "Ph 2-a dermoscopic image database for research and benchmarking," in *EMBC*. IEEE, 2013, pp. 5437–5440.
- [49] Y.-B. Tang, Y.-X. Tang, J. Xiao, and R. M. Summers, "Xlsor: A robust and accurate lung segmentor on chest x-rays using criss-cross attention and customized radiorealistic abnormalities generation," in *MIDL*. PMLR, 2019, pp. 457–467.
- [50] A. Hoover and M. Goldbaum, "Locating the optic nerve in a retinal image using the fuzzy convergence of the blood vessels," *IEEE Trans. Med. Imaging*, vol. 22, no. 8, pp. 951–958, 2003.
- [51] D. Vázquez, J. Bernal, F. J. Sánchez, G. Fernández-Esparrach, A. M. López, A. Romero, M. Drodzdzal, and A. Courville, "A benchmark for endoluminal scene segmentation of colonoscopy images," *J. Healthc. Eng.*, vol. 2017, no. 1, p. 4037190, 2017.
- [52] W. Al-Dhabyani, M. Gomaa, H. Khaled, and A. Fahmy, "Dataset of breast ultrasound images," *Data in brief*, vol. 28, p. 104863, 2020.
- [53] P. Naylor, M. Laé, F. Reyat, and T. Walter, "Segmentation of nuclei in histopathology images by deep regression of the distance map," *IEEE Trans. Med. Imaging*, vol. 38, no. 2, pp. 448–459, 2018.
- [54] J. Chen, J. Mei, X. Li, Y. Lu, Q. Yu, Q. Wei, X. Luo, Y. Xie, E. Adeli, Y. Wang *et al.*, "Transunet: Rethinking the u-net architecture design for medical image segmentation through the lens of transformers," *Med. Image Anal.*, p. 103280, 2024.